Surface reduction stabilizes single-crystalline Ni-rich layered cathode for Li-ion batteries

*Qinglu Fan,[†] Mateusz Jan Zuba, [‡] Yanxu Zong,[‡], Ashok Menon,[§] Anthony T. Pacileo,[†] Louis F.J. Piper,[‡,§] Guangwen Zhou, [‡,⊥] and Hao Liu [†, ‡,]**

[†]Department of Chemistry, Binghamton University, 4400 Parkway East, Binghamton, NY 13902, USA

[‡]Materials Science and Engineering, Binghamton University, 4400 Parkway East, Binghamton, NY 13902, USA

[§]WMG, University of Warwick, Coventry, CV4 7AL, UK

[⊥]Department of Mechanical Engineering, Binghamton University, 4400 Parkway East, Binghamton, NY 13902, USA

KEYWORDS. Single-crystalline NMC, surface modification

ABSTRACT. The surface of the layered transition metal oxide cathode plays an important role in its function and degradation. Modification of the surface structure and chemistry is often necessary to overcome the debilitating effect of the native surface. Here, we employ a chemical reduction method using CaI_2 to modify the native surface of single-crystalline layered transition metal oxide cathode particles. High-resolution transmission electron microscopy shows the

formation of a conformal cubic phase at the particle surface, where the outmost layer is enriched with Ca. The modified surface significantly improves the long-term capacity retention at low rates of cycling, yet the rate capability is compromised by the impeded interfacial kinetics at high voltages. The lack of oxygen vacancy generation in the chemically induced surface phase transformation likely results in a dense surface layer that accounts for the improved electrochemical stability and impeded Li-ion diffusion. This work highlights the strong dependence of the electrode's (electro)chemical stability and intercalation kinetics on the surface structure and chemistry, which can be further tailored by the chemical reduction method.

Introduction

The classical lithium layered transition metal oxides constitute an important class of cathode materials for Li-ion batteries.[1,2] The state-of-the-art Ni-rich $LiNi_xMn_yCo_{1-x-y}O_2$ (NMC) promises a high specific capacity of ~270 mAh/g based on the reversible intercalation of one Li ion per formula unit. Although nearly full Li extraction can be achieved in the initial cycle, the rapid capacity degradation in subsequent cycles restricts the practical reversible capacity to ~80% of the theoretical limit.[3] Recent mechanistic studies of the degradation process have revealed instabilities both at the surface and in the bulk of the NMC particles. The surface degradation suffers from the irreversible structural reconstruction at high voltages,[4] oxygen evolution,[5] transition metal ion dissolution,[6] while inter- and intra-granular cracking induced by the anisotropic lattice change[7] and layer gliding[8] contribute to bulk degradation. Further compounding the degradation process is the coupling between the surface and the bulk degradation. For example, the NiO-like surface layer has been proposed to cause the bulk fatigue of NMC single crystals,[9] and cracks in the bulk expose additional surfaces that invite further

surface degradation. Therefore, a stable surface is paramount for maintaining the long-term cycling stability of the electrode.

Surface modification provides a promising and effective strategy to increase surface stability, most notably, by introducing an additional layer between the electrolyte and the electrode.[10] The coating layer has been reported to serve multiple purposes, such as scavenging HF,[11] stabilizing the cathode-electrolyte interface,[12] improving the thermal stability,[13] and suppressing gas evolution.[14] Conventionally, the surface coating is performed via co-precipitation, sol-gel, hydrothermal, or solid-state methods. These methods typically involve an initial step to introduce the precursor of coating materials to the electrode surface, followed by a calcination step to transform the precursor to the desired coating material. While these methods are easy to implement with a broad range of chemistries, the homogeneity and thickness cannot be precisely controlled. The high-temperature calcination step can potentially modify the bulk structure of the electrode, for example, through the diffusion of the coating species into the bulk.[15] Therefore, the conventional coating methods may not be limited only to the modification of the surface. Deposition methods offer an alternative to directly depositing the desired coating material on the electrode surface without risking changes in the bulk properties. Among the various deposition techniques, atomic layer deposition emerges as an effective method to enable conformal coating with precise control of the chemistry and thickness of the coating layer.[16] Recent works employing atomic layer deposition for surface coatings of Al_2O_3[17–19] and ZrO_2[17,20] have demonstrated improved capacity retention for both poly- and single-crystalline NMC electrode particles. This underlines the role of conformal surface coating in stabilizing the long-term cycling of NMC electrodes.

Here, we employed a chemical redox reaction to modify the surface of a single-crystalline $LiNi_{0.83}Mn_{0.06}Co_{0.11}O_2$ (SX-NMC). This redox method induces a conversion reaction at the SX-NMC particle surface, which transforms into a dense NiO-like cubic phase. Notwithstanding the apparent similarity with the electrochemically induced surface transformation and the impeded interfacial reaction kinetics, this chemical transformation obviates the generation of the oxygen vacancies and leads to improved capacity retention over long-term cycling.

Experimental Methods

Preparation of oxidized single-crystalline NMC. The single-crystalline $LiNi_{0.83}Mn_{0.06}Co_{0.11}O_2$ (SX-NMC) was purchased from Ruyuan East Sunshine Magnetic Materials Co., Ltd. The oxidation of SX-NMC was performed by the reaction of SX-NMC powder with liquid bromine in a round-bottom flask. Excess bromine was used for this reaction. The molar ratio between bromine and SX-NMC was 10:1. The mixture was stirred overnight at room temperature to assure complete reaction. After the reaction, the resulting powder was recovered by centrifuge and washed several times with anhydrous acetonitrile until the liquid became clear to assure the complete removal of bromine. The powder was finally dried under vacuum at 65 ℃. This oxidized SX-NMC is denoted as Br-NMC.

Preparation of reduced SX-NMC. CaI_2 (VWR) was used as the reducing agent to reduce Br-NMC. In a typical experiment, 0.0905 g CaI_2 was added to 10 mL anhydrous acetonitrile in a 20 mL vial, which was covered with aluminum foil to avoid the decomposition of CaI_2 through light exposure. The mixture was sonicated and stirred for 15 min to ensure the complete dissolution of CaI_2. The CaI_2 solution was light pink. Then 0.6 g Br-NMC powder was added into the CaI_2 solution and stirred at 65 ℃ for two days. The color of the solution started to turn brown only a few minutes after the addition of the Br-NMC powder. A brown suspension was obtained after

two days of reaction. The resulting powder was recovered and thoroughly washed with anhydrous acetonitrile until the liquid became clear. The powder was then dried under vacuum at 65 °C and is denoted as Ca-NMC.

Electrode preparation and electrochemical characterization. The electrochemical properties of SX-NCM, Br-NMC and Ca-NMC were evaluated in CR2032 coin cells. The cell was assembled in an Ar-filled glovebox (O_2 < 0.5 ppm, H_2O < 0.5 ppm) with SX/Br/Ca-NMC as the cathode, lithium metal discs as the anode, the glass fiber as the separator, and the 1M $LiPF_6$ in 1:1 (volume ratio) ethylene carbonate/dimethyl carbonate solution (Gotion) as the electrolyte. The cathode was prepared by pressing the mixed powder of the active cathode material, carbon black, and polyvinylidene difluoride (PVDF) in 8:1:1 weight ratio at 50 psi in a die with a 10 mm diameter hole. The typical areal loading of the active material was ~15 mg/cm^2. To evaluate the long-term cycling performance of these samples, the cells were cycled at C/20 (1C = 200 mA/g) between 2.7-4.5 V for 2 cycles followed by 100 cycles at C/10. For the partially delithiated samples (i.e., Br-NMC and Ca-NMC), discharge was conducted first during the initial cycle. The rate capability of SX-NMC and Ca-NMC was measured for different current densities from C/10 to 5C between 2.7-4.5 V. All the cycling tests were conducted with the LANHE CA2100 cycler.

Measurement of the SX-NMC and Ca-NMC electrodes with the potentiostatic intermittent titration technique (PITT) was performed on a Biologic BCS-805 potentiostat in voltage steps of 10 mV during both charge and discharge in the voltage window of 2.7 – 4.5 V. The voltage was held constant at each step until the current decreased to 0.01C. The active mass loading of the electrode for the potentiostatic titration technique (PITT) measurement was ~ 5 mg/cm^2 to

minimize the current density and polarization. The chronoamperometry data (I(t)) for each potentiostatic step was fitted with Equation (1) assuming a finite interfacial kinetics,[21]

$$I(t) = -\frac{3DQ}{r^2}\left\{-\frac{B}{B-1}\left(1 - erfc\frac{r}{\sqrt{Dt}}\right) + \frac{B^2}{B-1}exp\left[\frac{Dt}{r^2}(B-1)^2\right]erfc\left[(B-1)\sqrt{\frac{Dt}{r^2}}\right] + \right.$$

$$\left.\frac{B^2-2B}{B-1}exp\left[2(B-1) + \frac{Dt}{r^2}(B-1)^2\right]erfc\left[\frac{r}{\sqrt{Dt}} + (B-1)\sqrt{\frac{Dt}{r^2}}\right]\right\} \quad (1)$$

where D is the Li-ion diffusivity, R the radius of the electrode particle, Q the total charge transferred during the potential step for the whole electrode, B the Biot number. Both B and D are fitting parameters. The exchange current density is derived from Equation (2),[22]

$$j_0 = -\frac{BDRT}{r\frac{\partial U}{\partial C}} \quad (2)$$

where B and D are the Biot number and Li-ion diffusivity , respectively, obtained from Equation (1), R is the universal gas constant, T is the temperature, r is the particle radius (estimated to be 1 μm), and $\frac{\partial U}{\partial C}$ is the derivative of the cell voltage (U) with respect to the Li-ion concentration (C) in the NMC particle, which is obtained from the voltage vs capacity curve for NMC.

Electrochemical impedance spectroscopy (EIS) measurement. EIS measurement of SX-NMC and Ca-NMC half cells at different stages of charge was conducted on an IviumStat electrochemical workstation in the frequency range from 0.0005 to 100 kHz. The cells were measured at fully charged state (4.5 V) and discharged state (2.7 V) at the 10th cycle.

X-ray powder diffraction. The X-ray powder diffraction measurement was performed on a Bruker D8 Advance X-ray diffractometer with Mo Kα radiation. Diffraction patterns were collected between 6-45° 2θ. The *operando* XRD measurement was performed with the same diffractometer using a homemade *operando* cell in the transmission geometry. Diffraction

patterns within 6-40° 2θ were continuously measured as the battery cell underwent galvanostatic cycling at 15 mA/g. The measurement of each pattern took 23 mins. Rietveld refinement was performed with Topas Academic v6.[23]

Electron microscopy. High-resolution transmission electron microscopy (HRTEM) imaging was carried out on JEOL JEM 2100F operated at 200 kV. The HRTEM sample preparation by Focused Ion Beam (FIB) was conducted on a Dual Beam Scanning Electron/FIB Microscope (FEI Helios) operated at 2-30 kV. Scanning transmission electron microscopy （STEM） images and Energy Dispersive X-ray spectroscopy （EDS） elemental maps were acquired with Thermo-Fischer Talos F200X at an accelerating voltage of 200 kV. Analysis of the HRTEM images (i.e., fast Fourier transform and Bragg filtering) was performed with CrysTBox.[24,25]

X-ray photoelectron spectroscopy (XPS). XPS was performed using a Phi VersaProbe 5000 system with a monochromated Al Kα source and hemispherical analyzer at the Analytical and Diagnostics Laboratory (ADL) at Binghamton University. All the samples were mounted on conductive carbon tape. Uncycled powder samples were also mixed with graphite where the corresponding C 1s peak at 284.5 eV was used for calibration. The core-levels (O 1s, Ni 2p, and Ca 2p) were measured with a pass energy of 23.5 eV.

X-ray absorption near edge spectroscopy (XANES). Ni K-edge X-ray absorption near edge structure data of the NMC powders were collected on an easyXAFS300+ spectrometer. The basic design and operation of the instrument can be found in Jahrman et al.[26] In brief, the measurement was performed in transmission mode using a silver X-ray source operated at 35 kV and 20 mA. The required energy range was accessed using a Si 551 spherically bent crystal analyzer (SBCA). A helium chamber was used in the X-ray flight path to reduce air scattering of

the X-rays. Measurements were made between 8300–8600 eV with a step size of 0.25 eV. For the experiment, ~20 mg of the powders was pressed into pellets using cellulose as the diluent (1:2 weight ratio), which were then stuck onto Kapton tape. The raw data were normalized using the empty beam. The energy was calibrated using metallic Ni foil with the instrument software. The subsequent pre-edge background subtraction and post-edge normalization were carried out using Athena.[27]

Elemental analysis. Elemental analysis was performed with a Varian VISTA MPX inductively coupled plasma-optical emission spectrometer (ICP-OES).

Results and discussion

Surface reduction of single-crystalline (SX) NMC. The SX-NMC was characterized by XRD and ICP to validate its phase purity and chemical composition. The XRD pattern shows a single phase corresponding to the layered lithium metal oxide (space group $R\bar{3}m$). The refined lattice parameters (a = 2.87473(2) Å, c = 14.1966(1) Å) are consistent with the reported values for Ni-rich NMCs. The refinement of the Li/Ni anti-site disorder yields 2.5(1)%. (**Figure S1 and Table S1**) The chemical composition obtained from ICP corresponds to Ni:Mn:Co = 83:5:12. The SX-NMC sample recovered after the bromine oxidation (denoted as Br-NMC) shows substantial changes in the lattice parameter (a = 2.82681(4) Å, c = 14.4696(3) Å, **Figure 1A**), which is consistent with the extraction of ~0.5 Li per formula unit (f.u.) of NMC based on the *operando* XRD measurement of the first charge of SX-NMC. (**Figure S2**) The exact Li composition of Br-NMC was determined by ICP, which yields 0.57 Li per f.u. of NMC for Br-NMC. The XANES of the Ni K-edge for Br-NMC is also observed to shift to higher energy, which is consistent with the oxidation of Ni ions. (**Figure 1B**)

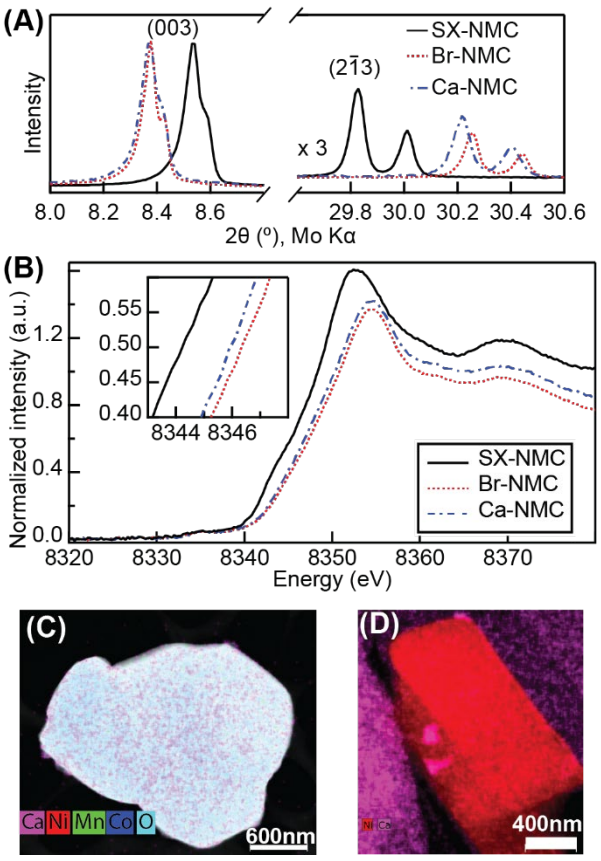

Figure 1.(A) (003) and (2$\bar{1}$3) reflections observed for the single-crystal NMC (SX-NMC), the NMC after oxidation by Br_2 (Br-NMC), and the NMC reduced by CaI_2 (Ca-NMC). The doublet arises from $K\alpha_1$ and $K\alpha_2$ radiations of Mo. **(B)** X-ray absorption spectra of the Ni K-edge for SX-NMC, Br-NMC, Ca-NMC. The shifts in the position of the Bragg peaks and the position of the Ni K-edge are consistent with the oxidation and reduction reactions in NMC. **(C)** Elemental mapping of a single Ca-NMC particle showing the homogenous distribution of Ca. **(D)** Elemental mapping of Ca at the FIB cross-section of a single Ca-NMC particle.

The reaction of CaI_2 with the partially delithiated Br-NMC led to a small but significant shift of the (2$\bar{1}$3) reflection to a lower angle. (**Figure 1A,** structural information in **Figure S3 and Table S2**) The *a* lattice parameter (a = 2.82994 Å) of the CaI_2-reacted sample, denoted as Ca-NMC hereafter, (structural information in **Figure S4** and **Table S3**) increases from that of Br-

NMC by 0.0027 Å, which corresponds to the reduction of the transition metal ions in the bulk. This observation is corroborated by the small shift of the Ni K-edge to lower energy, which is consistent with the Ni reduction in the bulk. (**Figure 1B**) Elemental analysis by ICP did not yield reliable concentration results for Ca because of the disparate concentration ranges required by the ICP instrument for the simultaneous quantification of the transition metal ions (0.004 – 20 ppm) and Ca ions (0.17 – 1000 ppm). Hence, the elemental analysis was conducted by EDX mapping of a single Ca-NMC particle, which shows the homogeneous distribution of Ca. (**Figure 1C**, the energy dispersive X-ray spectrum in **Figure S5**) Meanwhile, no Ca was detected in the particle cross-section produced by FIB. (**Figure 1D**) Therefore, the Ca ions are only distributed on the particle surface, and the reduction of the transition metal ions in the bulk is not due to the Ca-ion intercalation into the particle interior.

To interrogate the changes on the particle surface and elucidate the charge compensation mechanism in Ca-NMC, we employed XPS to examine the pristine NMC, Br-NMC, and Ca-NMC. The Ni $2p_{3/2}$ spectrum of the pristine NMC exhibits the main peak at 855 eV and a satellite peak at 862 eV, (**Figure 2A**) which are characteristic of the NMC compounds (e.g., NMC111, 532, 622, 811).[28] A recent study on the analysis of the Ni 2p spectra for a variety of NMC samples has assigned the main peak (855 eV) to a mixture of Ni^{2+} and Ni^{3+} species and the satellite peak (862 eV) exclusively to Ni^{2+} (as in NiO).[28] After the oxidation by Br_2, the average oxidation state of Ni ions in Br-NMC is +3.45, based on the stoichiometry of $Li_{0.57}Ni_{0.83}Mn_{0.05}Co_{0.12}O_2$ determined by the ICP elemental analysis and the formal oxidation states of +4 and +3 for Mn and Co ions, respectively.[29] Accordingly, the main Ni $2p_{3/2}$ peak shifts to the higher binding energy at 856 eV, with an attenuated satellite peak at 862 eV. This is consistent with the more oxidized surface of Br-NMC than SX-NMC. The reaction of Br-NMC

with CaI_2 leads to a recovery of the same Ni $2p_{3/2}$ spectrum as observed for the pristine SX-NMC, with the main and satellite peaks at 855 eV and 862 eV, respectively. Quantitative analysis of the oxidation state of Ni ions via the method by Bondarchuk *et al.*[28] yields a $Ni^{2+}/(Ni^{2+}+ Ni^{3+})$ fraction of 36% for Ca-NMC, which is similar to the surface $Ni^{2+}/(Ni^{2+}+ Ni^{3+})$ fraction measured for the pristine SX-NMC (41%). In contrast, the average oxidation state of Ni ions in Ca-NMC is +3.6. Therefore, the Ni ions on the surface are more reduced than those in the bulk for Ca-NMC. The Ca 2p peaks are also observed for Ca-NMC, **(Figure 2B)** validating the presence of Ca-containing species on the particle surface.

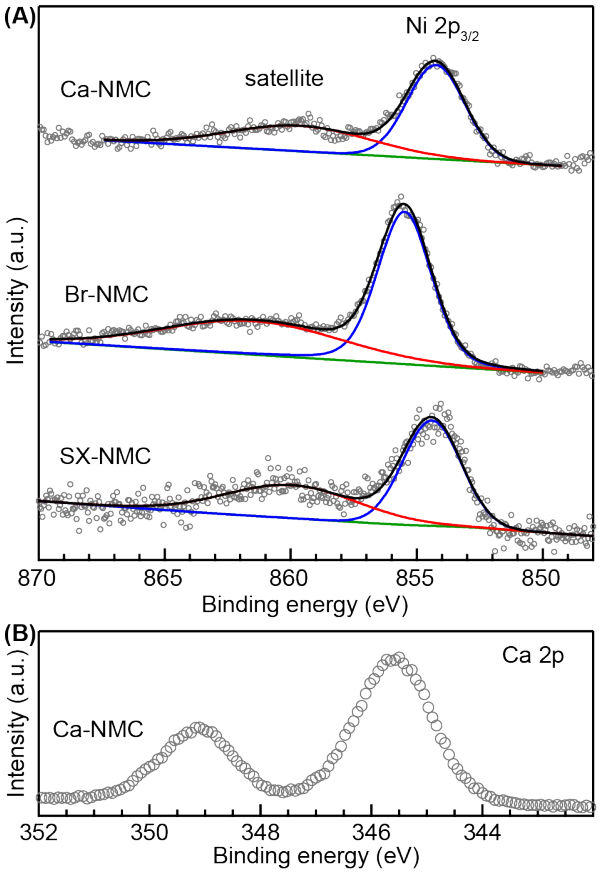

Figure 2. (A) Ni $2p_{3/2}$ XPS spectra observed for the single-crystalline NMC (SX-NMC), the NMC oxidized by Br_2 (Br-NMC), and the chemically reduced Br-NMC by CaI_2 (Ca-NMC) powder. **(B)** Ca 2p spectrum observed for Ca-NMC powder.

There are two mechanisms by which the surface reduction by CaI_2 can occur: (i) the intercalation of Ca ions into the interlayer space, or (ii) the conversion of the layered surface into simple oxides (e.g., Ca + MO_2 → CaO + MO, M = transition metal).[30] Mechanism (i) will preserve the layered structure, whereas mechanism (ii) will mostly likely transform the layered structure into the cubic phases adopted by many simple binary metal oxides, such as NiO and CaO. To differentiate the two mechanisms, we performed the HRTEM measurement for Ca-NMC. (**Figure 3A**) Since all the Bragg peaks from the cubic phase can also be indexed by the layered rhombohedral phase, only the Bragg peaks exclusively indexed by the rhombohedral phase can be used to characterize the layered phase. Here, the subscripts "C" and "R" are used in the Miller indices to denote the cubic and the rhombohedral phases, respectively, by which the Bragg peaks are indexed. Since the $(003)_R$ peak exclusively arises from the rhombohedral phase and is absent in the cubic phase, (**Figure 3B)** the $(003)_R$ Bragg filtered image is obtained to visualize the domain of the layered phase only. (**Figure 3C**) The fringes of the $(003)_R$ planes are found to extend from the particle interior to only ~5 nm beneath the particle surface, which demonstrates the absence of the layered phase at the particle surface. In contrast, the fringes in the $(006)_R/(111)_C$ Bragg filter image extend all the way to the particle surface. (**Figure 3D**) Hence, the fringes observed at the particle surface in **Figure 3D** can only be attributed to the cubic phase, i.e. the $(111)_C$ lattice planes. The observation of a ~5 nm cubic surface layer is consistent with the formation of the simple metal oxides, e.g., the cubic NiO and CaO, which agrees with the outcome based on mechanism (ii). This observation is consistent with the high Ca:Ni ratio measured by XPS (2:1 for Ca:Ni, **Table S4**), which can only be explained by the coverage of the particle surface with a layer of Ca-containing species, because the Ca:TM (TM = Ni, Co, and Mn) ratio cannot be greater than 1 for the layered structure with intercalated Ca ions.

Based on both the TEM and the XPS results, we conclude that the surface reduction by CaI_2 proceeds via the conversion mechanism.

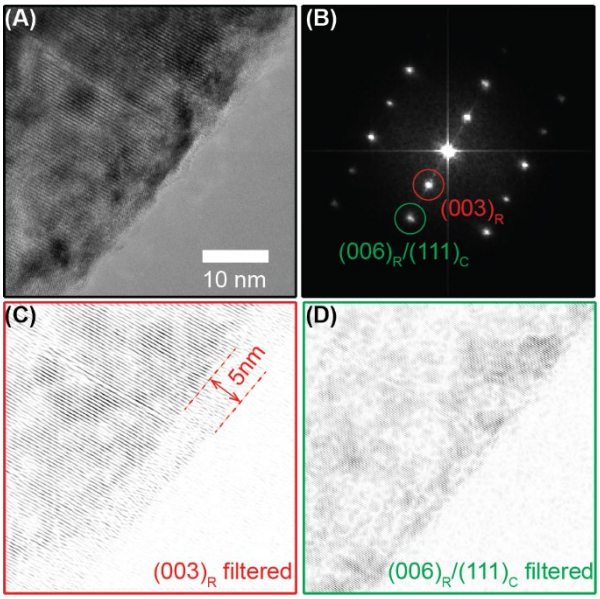

Figure 3. (A) High-resolution TEM image of a Ca-NMC particle, and **(B)** its diffractogram from fast Fourier transform. The subscript of the Miller index is used to denote the rhombohedral("R") or the cubic("C") phase by which the Bragg peak is indexed. The Bragg filtered images using **(C)** the $(003)_R$ reflection and **(D)** the $(006)_R/(111)_C$ reflection as indicated by the red and the green circles, respectively.

The conversion reaction is predicted by the density functional theory calculation to occur for a two-electron transfer per Ni ion with the intercalation of Ca ions in NiO_2, while the intercalation reaction is predicted for a one-electron transfer.[30,31] It is possible that the reaction with CaI_2 initially proceeds as the intercalation of Ca ions, but the high diffusion barrier of Ca ions in NiO_2[32] impedes the diffusion of Ca ions into the particle interior, leading to the accumulation of Ca ions at the surface. Once the surface concentration of Ca ions becomes sufficiently high, the conversion reaction occurs, resulting in the formation of a thin coating layer of CaO, which assumes the same cubic structure as NiO, and the displacement of Li ions into the particle

interior. The inward diffusion of Li ions increases the Li concentration of the bulk, resulting in changes in the measured lattice parameters. The proposed scheme for the reaction between Br-NMC and CaI_2 is illustrated in **Figure 4**.

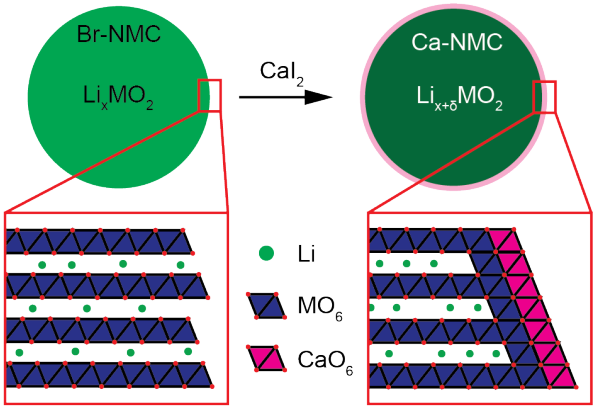

Figure 4. Schematic illustration of the chemical reduction of Br-NMC by CaI_2. The surface is transformed into cubic phases consisting of transition metal oxides (MO) and calcium oxide (CaO). The surface lithium is displaced into the interior to enrich the Li concentration in the bulk.

Effect of surface modification on electron and ion transport. The typical voltage profiles of SX-NMC and Ca-NMC for C/10 (1C = 200 mA/g) cycling between 2.7 V and 4.5 V, obtained after two slow cycles (same voltage window, C/20), are shown in **Figure 5A**. The reversible capacity of SX-NMC and Ca-NMC is 200 mAh/g and 193 mAh/g, respectively. The Ca-NMC electrode shows larger voltage hysteresis than SX-NMC in both the high (> 4.2 V) and low (< 3.6 V) voltage regions. The differential capacity (dQ/dV) vs. voltage plot is used to characterize the voltage hysteresis. (**Figure 5B**) Roman numerals are used to denote the dQ/dV peaks because these peaks do not necessarily correspond to structural phase transitions.[33] The hysteresis observed for Ca-NMC is primarily attributed to the overpotential of Peak I on charge (60 mV higher than SX-NMC) and Peak IV' on discharge (80 mV lower than SX-NMC). The differences in the positions of Peaks II, II', III, and III' between SX-NMC and Ca-NMC are only 5 mV. In

addition to the increased voltage hysteresis, the smearing of Peak IV on charge and the appearance of a long tail below 3.6 V on discharge are also observed for Ca-NMC. The differences between SX-NMC and Ca-NMC demonstrate the importance of surface in the electrochemical behavior of NMC electrodes.

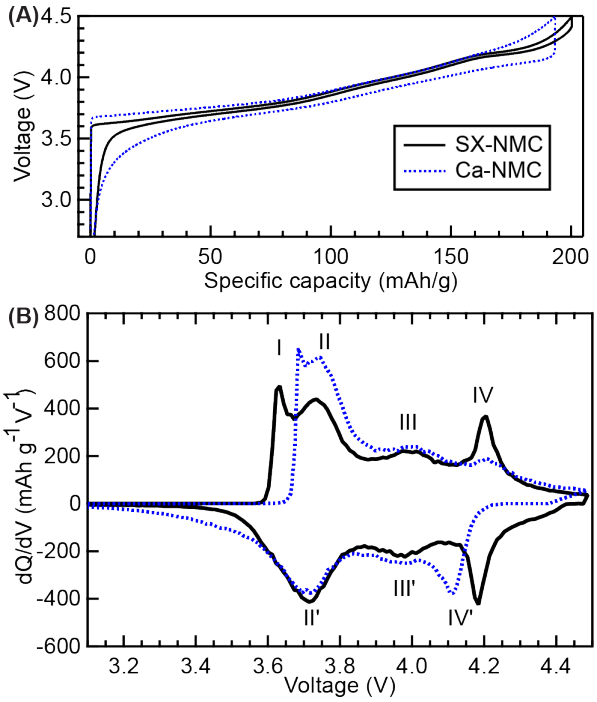

Figure 5. (A) Voltage profile of the pristine single-crystalline NMC (SX-NMC) and the Ca-modified NMC (Ca-NMC) during the 3rd cycle at 20 mA/g after 2 formation cycles, and **(B)** the corresponding differential capacity (dQ/dV) curves.

To further interrogate the effect of surface modification on the electron and ion transport kinetics, PITT was employed to characterize the Li-ion diffusion and the interfacial charge transfer resistance. The analysis of the PITT result was based on a finite interfacial kinetics model[21] that accounts for both the bulk Li-ion diffusivity and the exchange current density (j_0). (**Figure 6**) The parameter D/r^2, where D is the diffusivity and r the particle radius, is used instead of diffusivity to eliminate the ambiguity in estimating the radius (r) of the SX-NMC particles. Since the reaction with CaI_2 does not change the particle morphology, which is confirmed by SEM, (**Figure S6**) variation in the particle morphology is eliminated when comparing the results for the SX-NMC and Ca-NMC samples. The D/r^2 for Ca-NMC is consistently smaller than SX-NMC, which seems to suggest a decrease in the bulk Li-ion diffusion in Ca-NMC. However, the reaction with CaI_2 does not lead to any appreciable irreversible change in the bulk structure, specifically the Li-Ni anti-site defect concentration, which is relevant to the bulk Li-ion diffusion[34,35] and remains 1.8(7)% in Ca-NMC (full structural data available in **Table S3**), as opposed to 2.5(1)% in SX-NMC. Hence, the Li-ion diffusivity in the bulk crystal lattice is not expected to be affected by the surface modification. A recent ^{7}Li nuclear magnetic resonance measurement of the Li mobility in a pristine NMC and a heavily cycled NMC does not show a significant difference between the two.[9] It is recognized that the Li diffusivity is not the same at the surface, where the layered structure is transformed to the cubic NiO-like structure, and the bulk, yet the model adopted for analyzing the PITT data assumes a constant Li diffusivity throughout the entire particle. The assumption of uniform diffusivity in analyzing the kinetic electrochemical data has led to apparent discrepancies in the bulk diffusivity measurement for surface-modified samples, such as electrodes coated by the atomic layer deposition method,[36,37] which only changes the structure on the surface but not the bulk. Therefore, we attribute the

smaller Li diffusivity measured for the Ca-NMC to the impeded Li-ion diffusion through the surface layer.

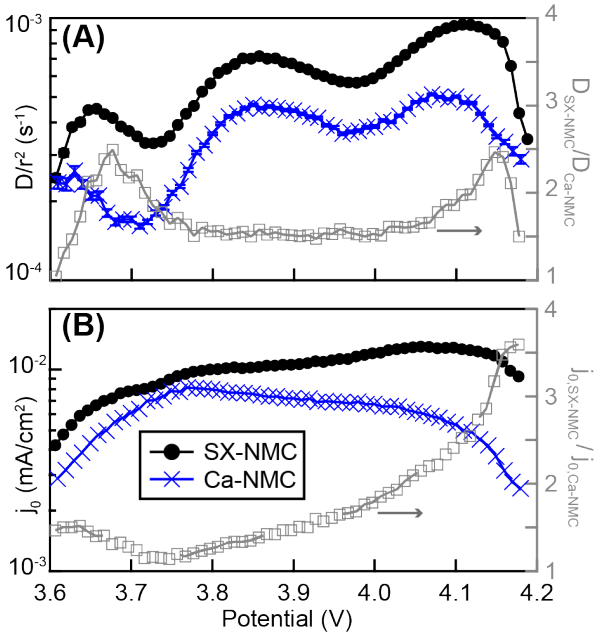

Figure 6. (A) Equivalent Li-ion diffusivity (D/r^2) and **(B)** exchange current density obtained from the PITT results for the SX-NMC (black) and the Ca-NMC (blue) electrodes.

The interfacial intercalation kinetics is characterized by the exchange current density, j_0. (**Figure 6B)** The exchange current density of SX-NMC increases from 4×10^{-3} mA/cm^2 at 3.6 V to 1.2×10^{-2} mA/cm^2 at 4.1 V and slightly decreases to 1×10^{-2} mA/cm^2 at 4.17 V. The appearance of a single maximum j_0 has also been observed for isolated $LiNi_{0.8}Co_{0.15}Al_{0.05}O_2$ (NCA) and $LiNi_{0.33}Mn_{0.33}Co_{0.33}O_2$ (NMC333) secondary particles measured by the same PITT method.[38,39] The j_0 values reported for NCA and NMC333 are one order of magnitude higher than the SX-NMC in this work, which may be caused by the microstructural difference between single crystals and secondary particles. The j_0 for Ca-NMC is consistently smaller than SX-NMC, with the maximum appearing at 3.75V. To compare the relative magnitude of j_0 for SX-NMC and Ca-NMC, the ratio, $j_{0,SX\text{-}NMC}/j_{0,Ca\text{-}NMC}$, is also plotted in **Figure 6B**. The ratio, $j_{0,SX\text{-}}$

$_{NMC}/j_{0,Ca\text{-}NMC}$, is less than 1.5 when the voltage is below 3.9 V but increases rapidly above 4.1 V, reaching 3.5 at close to 4.2 V. This disparity in j_0 between the two samples shows that the surface modification reduces the charge transfer kinetics more in the high voltage than in the low voltage region. This explains the observed lower potential (higher polarization) of the discharge dQ/dV peaks for Ca-NMC than for SX-NMC, where Peaks II', III', and IV' for Ca-NMC are lower by 5 mV, 5 mV, and 67 mV, respectively, than for SX-NMC. (**Figure 5B**) The small j_0 is consistent with the sluggish Li-ion mobility in the cubic phase at the surface of Ca-NMC particles. This observation is consistent with the larger charge transfer resistance measured by EIS for Ca-NMC than SX-NMC at both the charge and the discharged states. (**Figure S7**) Consequently, the rate capability of Ca-NMC is inferior to SX-NMC. (**Figure S8**)

Stability during long-term cycling. The long-term cycling was performed at C/10 (1C = 200 mA/g) for the pristine and Ca-NMC electrodes following two formation cycles (C/20 with 4.5 V upper cutoff). (**Figure 7A**) For the pristine SX-NMC, the discharge capacity decreases almost linearly from 200 mAh/g to 167 mAh/g after 100 cycles (83.5% capacity retention). For the Ca-NMC electrode cycled under the same condition, the discharge capacity first increases from 192 mAh/g at the 1st cycle to 195 mAh/g at the 25th cycle, followed by a monotonic decrease to 182 mAh/g at the 100th cycle (95% capacity retention). To elucidate whether the difference in the capacity retention is caused by the different initial discharge capacities, a Ca-NMC sample was cycled to 4.7 V cut-off voltage, which yields an initial discharge capacity of 210 mAh/g with 187 mAh/g retained after the 100th cycle (89% capacity retention). Even after controlling for the initial discharge capacity, the Ca-NMC sample demonstrates better capacity retention over long-term cycling than SX-NMC. It is observed that the oxidation by bromine increases the initial

discharge capacity but does not improve the cycling stability. Therefore, the stable cycling observed for Ca-NMC is due to the surface reduction by CaI_2, not the oxidation by bromine.

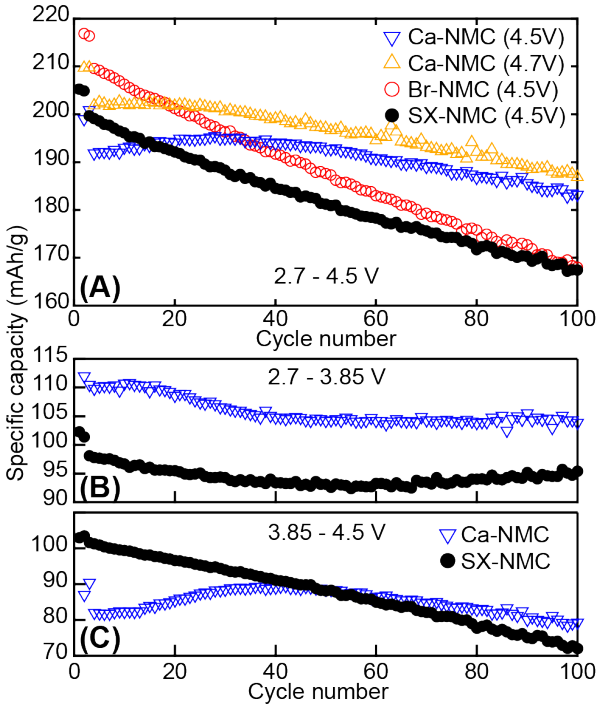

Figure 7. (A) Specific discharge capacities for SX-NMC (2.7-4.5 V), Ca-NMC (2.7-4.5 V and 2.7-4.7 V), and Br-NMC (2.7-4.5 V) at C/10. The first two cycles were performed at C/20. The specific discharge capacity is broken down into two voltage windows: **(B)** 2.7-3.85 V and **(C)** 3.85-4.5 V.

A breakdown of the discharge capacities obtained for the voltage windows of 2.7-3.85 V (**Figure 7B**) and 3.85-4.5 V (**Figure 7C**) shows that the disparity between SX-NMC and Ca-NMC arises primarily in the electrochemical processes above 3.85 V. For SX-NMC, the discharge capacity obtained above 3.85 V decreases monotonically from 102 mAh/g at the 3rd cycle to 72 mAh/g at the 100th cycle. For Ca-NMC, the capacity increases from 82 mAh/g at the 3rd cycle to 89 mAh/g at the 33rd cycle, followed by a gradual decrease to 79 mAh/g at the 100th cycle.

To further elucidate the electrochemical degradation, the differential capacity vs. voltage plot is obtained for the first 100 cycles (the first two C/20 cycles are excluded). (**Figure 8**) Notable changes of Peaks I/II/II' and Peaks IV/IV' are observed for both SX-NMC and Ca-NMC with increasing number of cycles. In the low-voltage regime (2.7-3.85 V), Peaks I and II' shift to higher and lower voltages, respectively, with increasing cycle number for SX-NMC. Yet, for Ca-NMC, Peak I initially shifts to lower voltages until the 30th cycle before it shifts to higher voltages. Although Peaks I and II appear at higher voltages in Ca-NMC than SX-NMC in the initial cycle, they remain at lower voltages in Ca-NMC than SX-NMC at the end of the long-term cycling, demonstrating the smaller voltage polarization on charge for Ca-NMC than for SX-NMC. Notably, Peaks I and II remain separated for Ca-NMC whereas both peaks coalesce for SX-NMC at the end of the 100th cycle. Peak II' on discharge also shows a more rapid shift to lower voltages with cycling in SX-NMC than Ca-NMC, which is characterized by the evolution of the Peak II' position. (**Figure 9A**) This shows the more rapid growth of polarization in SX-NMC than Ca-NMC, indicating the improved stability of Ca-NMC in the low voltage regime.

In the high-voltage regime, the position of Peaks IV and IV' is used to characterize the voltage polarization. (**Figure 9B**) For charge, Peak IV shifts from 4.20 V at the initial cycle to 4.23 V at the 100th cycle for SX-NMC but remains practically unchanged at 4.215 V for Ca-NMC. For discharge, Peak IV' decreases from 4.19 V to 4.09 V for SX-NMC while a transient increase from 4.12 V at the initial cycle to 4.16 V at the 37th cycle before a monotonic decrease to 4.12 V at the 100th cycle is observed for Ca-NMC. The polarization, which is determined as the difference between the positions of Peaks IV and IV', increases from 17 mV at the initial cycle to 140 mV at the 100th cycle for SX-NMC. In contrast, the polarization observed for Ca-NMC first decreases from 74 mV at the initial cycle to 46 mV at the 30th cycle and then increases to 90

mV at the 100th cycle. This demonstrates the stabilizing effect of the surface modification in the high-voltage regime, which is known to induce degradation of the particle surface.

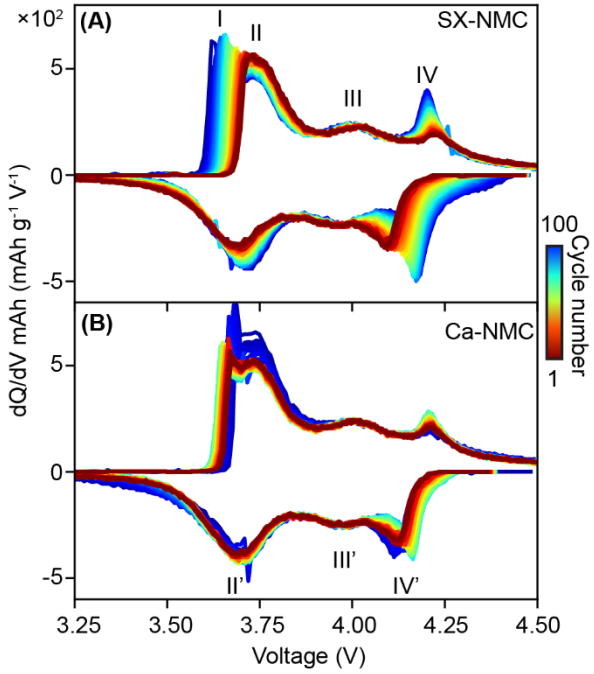

Figure 8. Differential capacity (dQ/dV) plot for **(A)** SX-NMC and **(B)** Ca-NMC during the first 100 cycles between 2.7 V and 4.5 V at C/10. The first two C/20 cycles before the long-term cycling at C/10 are omitted.

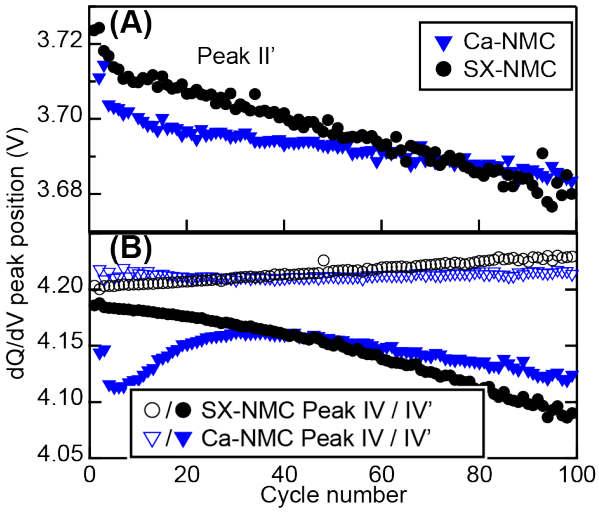

Figure 9. dQ/dV peak position as a function of the cycle number for **(A)** Peak II' and **(B)** Peaks IV and IV'. The peak position is obtained by fitting each dQ/dV peak with a Gaussian-shaped peak.

Evolution of the modified surface. Since the difference between SX-NMC and Ca-NMC is exclusively at the particle surface, the X-ray photoelectron spectra of Ca 2p and O 1s were measured for the cycled Ca-NMC electrodes harvested at the end of the 20th, 31st, and 100th cycles. The O 1s spectra (**Figure 10A**) are assigned to two different oxygen species – the lattice oxygen (bonded to metals) and the surface oxygen (such as in carbonates and hydroxides). The lattice oxygen is modelled with a single peak at 529.5 eV, and the surface oxygen is modelled with two peaks above 530 eV.[40–42] Both the lattice and surface oxygen species are observed for the samples harvested from the 20th and 31st cycles, but only the surface oxygen is observed for the sample harvested from the 100th cycle. For the Ca 2p spectra, the 2p3/2 and 2p1/2 doublet corresponding to CaO is observed for the samples harvested from the 20th and 31st cycles but not for the 100th cycle. (**Figure 10B**) To quantify the surface compositional changes, we normalized the composition of Ca and lattice oxygen (O_{met}) species against the overall oxygen species (O_{sum}). (**Figure 10C**) From the uncycled to the 20th cycle, the O_{met}/O_{sum} ratio remains practically constant. This indicates the lack of the cathode-electrolyte interphase (CEI) growth because the coverage of the particle surface with a CEI layer would have reduced the O_{met}/O_{sum} ratio.[43] Meanwhile, the Ca/O_{sum} ratio decreases from 0.14 for the uncycled Ca-NMC to 0.02 for the 20th cycle. Given the lack of significant CEI at the surface, this significant decrease in the Ca/O_{sum} ratio cannot be explained by the growth of a surface layer and is attributed to the partial removal of surface CaO. It is noted that this significant decrease in the Ca/O_{sum} ratio coincides with the significant reduction of voltage polarization observed for Peak IV' during discharge

(**Figure 9B**). The loss of surface CaO suggests CaO as a sacrificial agent that would be gradually consumed over time. It has been revealed from DFT calculations[11] that not all surface coating chemistries are stable against etching by HF in the electrolyte. For example, attenuation of the XPS Zn 2p signal was reported after 100 charge-discharge cycles for a $LiMn_2O_4$ electrode coated with ZnO by the atomic layer deposition method.[44] Further cycling to the 31st cycle results in a significant decrease of the O_{met}/O_{sum} ratio to 0.15, which is attributed to the growth of CEI at the surface of the electrode. On the other hand, the Ca/O_{sum} ratio remains constant, hence the decrease of O_{met}/O_{sum} is attributed to the attenuation of the O 2p signal from the lattice oxygen below the surface CaO layer. At the end of the 100th cycle, neither O_{met} nor Ca is observed, and only the surface oxygen species remain, which is attributed to the further growth of the CEI layer that completely covers the CaO and/or the transition metal oxide.[43]

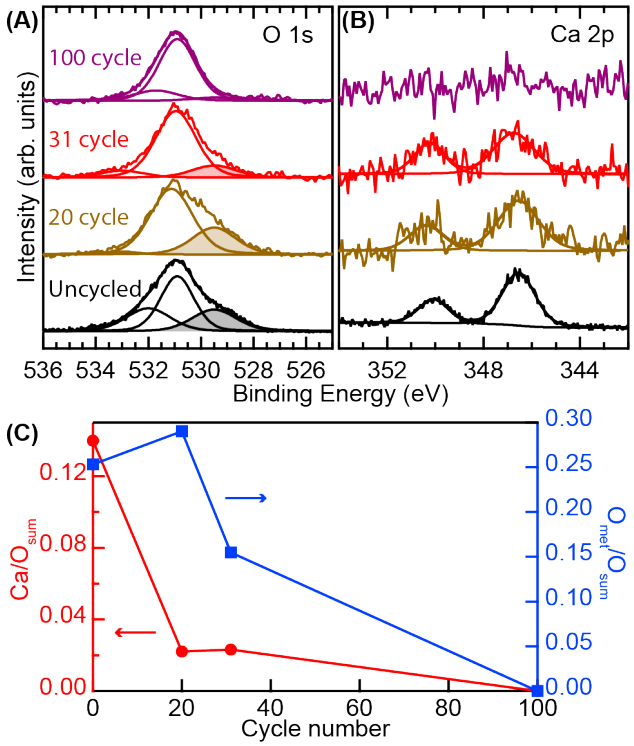

Figure 10. (A) O 1s and **(B)** Ca 2p X-ray photoelectron spectra measured for uncycled and cycled Ca-NMC electrodes. **(C)** Ratio between Ca and all oxygen species (Ca/O_{sum}) and the

proportion of lattice oxygen (O_{met}) in all oxygen bonds (O_{met}/O_{sum}) obtained from the quantitative analysis of the XPS result.

Discussion

The progressive surface transformation of the layered structure into the NiO-like rocksalt phase is a major cause of the long-term degradation of Ni-rich NMC cathodes,[9,45] and the thickness of the reconstructed surface of the pristine NCM cathode often serves as a good indicator for its electrochemical performance.[46,47] Yet, the rather thick (~5nm) cubic surface phase observed for Ca-NMC is correlated with improved capacity retention despite the sluggish interfacial kinetics at high voltages. It must be noted that the cubic surface phase observed for Ca-NMC is different from the one induced by electrochemical cycling at least in two aspects. First, the surface layer of Ca-NMC contains Ca that is absent in non-modified NMC. The loss of Ca during the initial cycles suggests the sacrificial role of the Ca-containing layer in the long-term cycling of Ca-NMC. Secondly, the cubic surface layer of Ca-NMC is formed via a different reaction path than that formed *in-situ* during electrochemical cycling. The conversion reaction induced by CaI_2 reduction does not involve the generation of oxygen vacancies, which likely results in a denser surface layer. In contrast, the electrochemically induced surface cubic phase is formed via cation migration and the generation of oxygen vacancies[48] that leads to the eventual release of the highly reactive singlet oxygen gas.[5] The accumulation of oxygen vacancies has been recognized to account for the continuous surface phase transition.[49] The lack of oxygen vacancies in the chemically induced surface layer can be beneficial for suppressing further degradation and transformation of the surface layer, which is evident in the slow increase of the voltage polarization over extended cycles. (**Figure 9)** Although the irreversible phase transition at the surface is generally considered detrimental to the cycling stability of NMC cathodes, the

effect of this surface transformation should be evaluated considering the chemistry and structure of the surface layer. For example, recent transmission electron microscopy[50] and first-principle simulation[51] studies have revealed in the electrochemically induced surface layer the presence of multiple off-stoichiometric phases, such as β-Ni_5O_8 and γ-Ni_3O_4, which exhibit different Li-ion transport kinetics. Therefore, altering the reaction pathway for the surface transformation, such as demonstrated in the present work, can be a promising strategy to improve the interfacial stability of Ni-rich NMC cathodes.

In addition to the modified surface transformation pathway, the chemical reduction method reported here provides a novel approach to introducing secondary chemical species conformally on the particle surface. Our preliminary results show increased polarization and voltage hysteresis for MgI_2-reduced SX-NMC compared to Ca-NMC. (**Figure S9A**) The iodide-reduction method was also performed for polycrystalline NMC811 (Targray) electrode particles, where the CaI_2-modified electrode outperforms the ones modified by MgI_2 and AlI_3 in both the voltage hysteresis and capacity retention. (**Figure S9B**) Although the origin of the differences between electrodes modified by different iodides is unclear and is beyond the scope of this work, it highlights the critical effect of surface chemistry on the electrochemical performance of Ni-rich layered oxides. To optimize this surface-modification method for high-performance cathode, it is necessary to anneal the chemically reduced samples at elevated temperatures. It must be noted that thermal treatment at elevated temperatures is often employed to yield high-performance electrode powders coated by other methods. For example, annealing at elevated temperatures (> 500 ºC) is often employed to further optimize the electrode powders coated by the atomic layer deposition.[17,20] However, the use of a highly oxidized NMC sample precludes the possibility of high-temperature annealing following the chemical reduction because of the

decreasing thermal stability of NMC with an increasing level of delithiation (oxidation).[52] A possible strategy to allow for annealing with the present method is to use only slightly oxidized NMC to increase the thermal stability of the chemically reduced sample.

Conclusions

We have implemented a chemical reduction method to exclusively modify the surface of single-crystalline NMC particles. The reduction of partially oxidized NMC particles by CaI_2 results in the formation of a cubic surface layer with high Ca content in the topmost layer. The surface transformation induced by chemical reduction does not generate oxygen vacancies that are necessary for the electrochemically induced surface transformation. This lack of oxygen vacancies is believed to underpin the improved long-term cycling stability despite the hindered interfacial kinetics at higher voltages. This chemical reduction method presents a novel strategy to tailor the structure and chemistry of the NMC particle surface for improved electrochemical performance.

ASSOCIATED CONTENT

Supporting Information. Powder XRD patterns for SX-NMC, Br-NMC, Ca-NMC, and Rietveld refined structural parameters; operando XRD patterns for the first charge-discharge of SX-NMC and the refined lattice parameters; EDX spectrum for Ca-NMC; SEM images of SX-NMC, Br-NMC, and Ca-NMC powders; EIS for SX-NMC and Ca-NMC; rate testing results for SX-NMC and Ca-NMC; electrochemistry for Mg-modified single crystal NMC and Mg-, Ca-, Al-modified polycrystalline NMC811 (PDF).

AUTHOR INFORMATION

Corresponding Author

*E-mail: liuh@binghamton.edu

Author Contributions

The manuscript was written through contributions of all authors. All authors have given approval to the final version of the manuscript.

Funding Sources

Start-up fund of Binghamton University; National Science Foundation; China Scholarship Council.

ACKNOWLEDGMENT

This work was supported by the start-up fund of Binghamton University and NSF CBET-2144296 and CBET- 2028722. QF acknowledges financial support from China Scholarship Council (201908440453).

ABBREVIATIONS

NMC, $LiNi_xMn_yCo_{1-x-y}O_2$; PITT, potentiostatic titration technique; XRD, X-ray diffraction; FIB, focused ion beam; HRTEM, high-resolution transmission electron microscopy; XPS, X-ray photoelectron spectroscopy; XANES, X-ray absorption near edge spectroscopy; ICP, inductively coupled plasma; EIS, electrochemical impedance spectroscopy; CEI, cathode-electrolyte interphase.

REFERENCES

(1) Manthiram, A. A Reflection on Lithium-Ion Battery Cathode Chemistry. *Nat. Commun.* **2020**, *11* (1), 1550. https://doi.org/10.1038/s41467-020-15355-0.

(2) Manthiram, A.; Goodenough, J. B. Layered Lithium Cobalt Oxide Cathodes. *Nat. Energy* **2021**, *6* (3), 323. https://doi.org/10.1038/s41560-020-00764-8.

(3) Li, H.; Liu, A.; Zhang, N.; Wang, Y.; Yin, S.; Wu, H.; Dahn, J. R. An Unavoidable Challenge for Ni-Rich Positive Electrode Materials for Lithium-Ion Batteries. *Chem. Mater.* **2019**, *31* (18), 7574–7583. https://doi.org/10.1021/acs.chemmater.9b02372.

(4) Lin, F.; Nordlund, D.; Weng, T.-C.; Zhu, Y.; Ban, C.; Richards, R. M.; Xin, H. L. Phase Evolution for Conversion Reaction Electrodes in Lithium-Ion Batteries. *Nat. Commun.* **2014**, *5* (1), 3358. https://doi.org/10.1038/ncomms4358.

(5) Wandt, J.; Freiberg, A. T. S.; Ogrodnik, A.; Gasteiger, H. A. Singlet Oxygen Evolution from Layered Transition Metal Oxide Cathode Materials and Its Implications for Lithium-Ion Batteries. *Mater. Today* **2018**, *21* (8), 825–833. https://doi.org/10.1016/j.mattod.2018.03.037.

(6) Asl, H. Y.; Manthiram, A. Reining in Dissolved Transition-Metal Ions. *Science (80-.).* **2020**, *369* (6500), 140–141. https://doi.org/10.1126/science.abc5454.

(7) Liu, H.; Wolf, M.; Karki, K.; Yu, Y.; Stach, E. A.; Cabana, J.; Chapman, K. W.; Chupas, P. J. Intergranular Cracking as a Major Cause of Long-Term Capacity Fading of Layered Cathodes. *Nano Lett.* **2017**, *17* (6), 3452–3457. https://doi.org/10.1021/acs.nanolett.7b00379.

(8) Bi, Y.; Tao, J.; Wu, Y.; Li, L.; Xu, Y.; Hu, E.; Wu, B.; Hu, J.; Wang, C.; Zhang, J.; Qi, Y.; Xiao, J. Reversible Planar Gliding and Microcracking in a Single-Crystalline Ni-Rich Cathode. *Science (80-.).* **2020**, *370* (6522), 1313–1317. https://doi.org/10.1126/science.abc3167.

(9) Xu, C.; Märker, K.; Lee, J.; Mahadevegowda, A.; Reeves, P. J.; Day, S. J.; Groh, M. F.; Emge, S. P.; Ducati, C.; Layla Mehdi, B.; Tang, C. C.; Grey, C. P. Bulk Fatigue Induced by

Surface Reconstruction in Layered Ni-Rich Cathodes for Li-Ion Batteries. *Nat. Mater.* **2021**, *20* (1), 84–92. https://doi.org/10.1038/s41563-020-0767-8.

(10) Kim, J. M.; Zhang, X.; Zhang, J. G.; Manthiram, A.; Meng, Y. S.; Xu, W. A Review on the Stability and Surface Modification of Layered Transition-Metal Oxide Cathodes. *Mater. Today* **2021**, *46* (June), 155–182. https://doi.org/10.1016/j.mattod.2020.12.017.

(11) Tebbe, J. L.; Holder, A. M.; Musgrave, C. B. Mechanisms of LiCoO 2 Cathode Degradation by Reaction with HF and Protection by Thin Oxide Coatings. *ACS Appl. Mater. Interfaces* **2015**, *7* (43), 24265–24278. https://doi.org/10.1021/acsami.5b07887.

(12) Chae, B. J.; Yim, T. Sulfonate-Immobilized Artificial Cathode Electrolyte Interphases Layer on Ni-Rich Cathode. *J. Power Sources* **2017**, *360*, 480–487. https://doi.org/10.1016/j.jpowsour.2017.06.037.

(13) Wu, Y.; Ming, H.; Li, M.; Zhang, J.; Wahyudi, W.; Xie, L.; He, X.; Wang, J.; Wu, Y.; Ming, J. New Organic Complex for Lithium Layered Oxide Modification: Ultrathin Coating, High-Voltage, and Safety Performances. *ACS Energy Lett.* **2019**, *4* (3), 656–665. https://doi.org/10.1021/acsenergylett.9b00032.

(14) Kim, Y. Encapsulation of LiNi0.5Co0.2Mn0.3O2 with a Thin Inorganic Electrolyte Film to Reduce Gas Evolution in the Application of Lithium Ion Batteries. *Phys. Chem. Chem. Phys.* **2013**, *15* (17), 6400. https://doi.org/10.1039/c3cp50567g.

(15) Xin, F.; Zhou, H.; Bai, J.; Wang, F.; Whittingham, M. S. Conditioning the Surface and Bulk of High-Nickel Cathodes with a Nb Coating: An In Situ X-Ray Study. *J. Phys. Chem. Lett.* **2021**, *12* (33), 7908–7913. https://doi.org/10.1021/acs.jpclett.1c01785.

(16) Jin, Y.; Yu, H.; Liang, X. Understanding the Roles of Atomic Layer Deposition in Improving the Electrochemical Performance of Lithium-Ion Batteries. *Appl. Phys. Rev.* **2021**, *8* (3), 031301. https://doi.org/10.1063/5.0048337.

(17) Gao, Y.; Park, J.; Liang, X. Comprehensive Study of Al- and Zr-Modified LiNi 0.8 Mn 0.1 Co 0.1 O 2 through Synergy of Coating and Doping. *ACS Appl. Energy Mater.* **2020**, *3* (9), 8978–8987. https://doi.org/10.1021/acsaem.0c01420.

(18) Negi, R. S.; Culver, S. P.; Wiche, M.; Ahmed, S.; Volz, K.; Elm, M. T. Optimized Atomic Layer Deposition of Homogeneous, Conductive Al 2 O 3 Coatings for High-Nickel NCM Containing Ready-to-Use Electrodes. *Phys. Chem. Chem. Phys.* **2021**, *23* (11), 6725–6737. https://doi.org/10.1039/D0CP06422J.

(19) Mohanty, D.; Dahlberg, K.; King, D. M.; David, L. A.; Sefat, A. S.; Wood, D. L.; Daniel, C.; Dhar, S.; Mahajan, V.; Lee, M.; Albano, F. Modification of Ni-Rich FCG NMC and NCA Cathodes by Atomic Layer Deposition: Preventing Surface Phase Transitions for High-Voltage Lithium-Ion Batteries. *Sci. Rep.* **2016**, *6* (February), 1–16. https://doi.org/10.1038/srep26532.

(20) Bao, W.; Qian, G.; Zhao, L.; Yu, Y.; Su, L.; Cai, X.; Zhao, H.; Zuo, Y.; Zhang, Y.; Li, H.; Peng, Z.; Li, L.; Xie, J. Simultaneous Enhancement of Interfacial Stability and Kinetics of Single-Crystal LiNi0.6Mn0.2Co0.2O2through Optimized Surface Coating and Doping. *Nano Lett.* **2020**, *20* (12), 8832–8840. https://doi.org/10.1021/acs.nanolett.0c03778.

(21) Li, J.; Yang, F.; Xiao, X.; Verbrugge, M. W.; Cheng, Y. T. Potentiostatic Intermittent Titration Technique (PITT) for Spherical Particles with Finite Interfacial Kinetics. *Electrochim. Acta* **2012**, *75*, 56–61. https://doi.org/10.1016/j.electacta.2012.04.050.

(22) Li, J.; Xiao, X.; Yang, F.; Verbrugge, M. W.; Cheng, Y. T. Potentiostatic Intermittent Titration Technique for Electrodes Governed by Diffusion and Interfacial Reaction. *J. Phys. Chem. C* **2012**, *116* (1), 1472–1478. https://doi.org/10.1021/jp207919q.

(23) Coelho, A. A. TOPAS and TOPAS-Academic: An Optimization Program Integrating Computer Algebra and Crystallographic Objects Written in C++: An. *J. Appl. Crystallogr.* **2018**, *51* (1), 210–218. https://doi.org/10.1107/S1600576718000183.

(24) Klinger, M. More Features, More Tools, More CrysTBox. *J. Appl. Crystallogr.* **2017**, *50* (4), 1226–1234. https://doi.org/10.1107/S1600576717006793.

(25) Klinger, M.; Jäger, A. Crystallographic Tool Box (CrysTBox): Automated Tools for Transmission Electron Microscopists and Crystallographers. *J. Appl. Crystallogr.* **2015**, *48* (2015), 2012–2018. https://doi.org/10.1107/S1600576715017252.

(26) Jahrman, E. P.; Holden, W. M.; Ditter, A. S.; Mortensen, D. R.; Seidler, G. T.; Fister, T. T.; Kozimor, S. A.; Piper, L. F. J.; Rana, J.; Hyatt, N. C.; Stennett, M. C. An Improved Laboratory-Based x-Ray Absorption Fine Structure and x-Ray Emission Spectrometer for Analytical Applications in Materials Chemistry Research. *Rev. Sci. Instrum.* **2019**, *90* (2), 024106. https://doi.org/10.1063/1.5049383.

(27) Ravel, B.; Newville, M. ATHENA, ARTEMIS, HEPHAESTUS: Data Analysis for X-Ray Absorption Spectroscopy Using IFEFFIT. *J. Synchrotron Radiat.* **2005**, *12* (4), 537–541. https://doi.org/10.1107/S0909049505012719.

(28) Bondarchuk, O.; LaGrow, A. P.; Kvasha, A.; Thieu, T.; Ayerbe, E.; Urdampilleta, I. On the X-Ray Photoelectron Spectroscopy Analysis of LiNixMnyCozO2 Material and Electrodes. *Appl. Surf. Sci.* **2021**, *535* (January), 147699. https://doi.org/10.1016/j.apsusc.2020.147699.

(29) Quilty, C. D.; West, P. J.; Wheeler, G. P.; Housel, L. M.; Kern, C. J.; Tallman, K. R.; Ma, L.; Ehrlich, S.; Jaye, C.; Fischer, D. A.; Takeuchi, K. J.; Bock, D. C.; Marschilok, A. C.; Takeuchi, E. S. Elucidating Cathode Degradation Mechanisms in LiNi 0.8 Mn 0.1 Co 0.1 O 2 (NMC811)/Graphite Cells Under Fast Charge Rates Using Operando Synchrotron Characterization. *J. Electrochem. Soc.* **2022**, *169* (2), 020545. https://doi.org/10.1149/1945-7111/ac51f5.

(30) Hannah, D. C.; Sai Gautam, G.; Canepa, P.; Ceder, G. On the Balance of Intercalation and Conversion Reactions in Battery Cathodes. *Adv. Energy Mater.* **2018**, *8* (20), 1–12. https://doi.org/10.1002/aenm.201800379.

(31) Park, H.; Bartel, C. J.; Ceder, G.; Zapol, P. Layered Transition Metal Oxides as Ca Intercalation Cathodes: A Systematic First-Principles Evaluation. *Adv. Energy Mater.* **2021**, *11* (48), 1–10. https://doi.org/10.1002/aenm.202101698.

(32) Rong, Z.; Malik, R.; Canepa, P.; Sai Gautam, G.; Liu, M.; Jain, A.; Persson, K.; Ceder, G. Materials Design Rules for Multivalent Ion Mobility in Intercalation Structures. *Chem. Mater.* **2015**, *27* (17), 6016–6021. https://doi.org/10.1021/acs.chemmater.5b02342.

(33) Xu, C.; Reeves, P. J.; Jacquet, Q.; Grey, C. P. Phase Behavior during Electrochemical Cycling of Ni-Rich Cathode Materials for Li-Ion Batteries. *Adv. Energy Mater.* **2021**, *11* (7), 2003404. https://doi.org/10.1002/aenm.202003404.

(34) Kang, K.; Ceder, G. Factors That Affect Li Mobility in Layered Lithium Transition Metal Oxides. *Phys. Rev. B - Condens. Matter Mater. Phys.* **2006**, *74* (9), 1–7. https://doi.org/10.1103/PhysRevB.74.094105.

(35) Zhao, E.; Fang, L.; Chen, M.; Chen, D.; Huang, Q.; Hu, Z.; Yan, Q. B.; Wu, M.; Xiao, X. New Insight into Li/Ni Disorder in Layered Cathode Materials for Lithium Ion Batteries: A Joint Study of Neutron Diffraction, Electrochemical Kinetic Analysis and First-Principles Calculations. *J. Mater. Chem. A* **2017**, *5* (4), 1679–1686. https://doi.org/10.1039/c6ta08448f.

(36) Zhu, Y.; Pham, H.; Park, J. A New Aspect of the Li Diffusion Enhancement Mechanism of Ultrathin Coating Layer on Electrode Materials. *ACS Appl. Mater. Interfaces* **2019**, *11* (42), 38719–38726. https://doi.org/10.1021/acsami.9b12740.

(37) Li, X.; Liu, J.; Banis, M. N.; Lushington, A.; Li, R.; Cai, M.; Sun, X. Atomic Layer Deposition of Solid-State Electrolyte Coated Cathode Materials with Superior High-Voltage Cycling Behavior for Lithium Ion Battery Application. *Energy Environ. Sci.* **2014**, *7* (2), 768–778. https://doi.org/10.1039/c3ee42704h.

(38) Tsai, P.-C.; Wen, B.; Wolfman, M.; Choe, M.-J.; Pan, M. S.; Su, L.; Thornton, K.; Cabana, J.; Chiang, Y.-M. Single-Particle Measurements of Electrochemical Kinetics in NMC and NCA Cathodes for Li-Ion Batteries. *Energy Environ. Sci.* **2018**, *11* (4), 860–871. https://doi.org/10.1039/C8EE00001H.

(39) Wen, B.; Deng, Z.; Tsai, P.-C.; Lebens-Higgins, Z. W.; Piper, L. F. J.; Ong, S. P.; Chiang, Y.-M. Ultrafast Ion Transport at a Cathode–Electrolyte Interface and Its Strong Dependence on Salt Solvation. *Nat. Energy* **2020**, *5* (8), 578–586. https://doi.org/10.1038/s41560-020-0647-0.

(40) Baggetto, L.; Dudney, N. J.; Veith, G. M. Surface Chemistry of Metal Oxide Coated Lithium Manganese Nickel Oxide Thin Film Cathodes Studied by XPS. *Electrochim. Acta* **2013**, *90*, 135–147. https://doi.org/10.1016/j.electacta.2012.11.120.

(41) Lebens-Higgins, Z. W.; Sallis, S.; Faenza, N. V.; Badway, F.; Pereira, N.; Halat, D. M.; Wahila, M.; Schlueter, C.; Lee, T.-L.; Yang, W.; Grey, C. P.; Amatucci, G. G.; Piper, L. F. J. Evolution of the Electrode–Electrolyte Interface of LiNi0.8Co0.15Al0.05O2 Electrodes Due to Electrochemical and Thermal Stress. *Chem. Mater.* **2018**, *30* (3), 958–969. https://doi.org/10.1021/acs.chemmater.7b04782.

(42) Lu, Y.-C.; Mansour, A. N.; Yabuuchi, N.; Shao-Horn, Y. Probing the Origin of Enhanced Stability of "$AlPO_4$" Nanoparticle Coated $LiCoO_2$ during Cycling to High Voltages: Combined XRD and XPS Studies. *Chem. Mater.* **2009**, *21* (19), 4408–4424. https://doi.org/10.1021/cm900862v.

(43) Zhang, Z.; Yang, J.; Huang, W.; Wang, H.; Zhou, W.; Li, Y.; Li, Y.; Xu, J.; Huang, W.; Chiu, W.; Cui, Y. Cathode-Electrolyte Interphase in Lithium Batteries Revealed by Cryogenic Electron Microscopy. *Matter* **2021**, *4* (1), 302–312. https://doi.org/10.1016/j.matt.2020.10.021.

(44) Zhao, J.; Wang, Y. Ultrathin Surface Coatings for Improved Electrochemical Performance of Lithium Ion Battery Electrodes at Elevated Temperature. *J. Phys. Chem. C* **2012**, *116* (22), 11867–11876. https://doi.org/10.1021/jp3010629.

(45) Lin, F.; Markus, I. M.; Nordlund, D.; Weng, T.-C.; Asta, M. D.; Xin, H. L.; Doeff, M. M. Surface Reconstruction and Chemical Evolution of Stoichiometric Layered Cathode Materials for Lithium-Ion Batteries. *Nat. Commun.* **2014**, *5* (1), 3529. https://doi.org/10.1038/ncomms4529.

(46) Kim, M.; Zhu, J.; Li, L.; Wang, C.; Chen, G. Understanding Reactivities of Ni-Rich Li[Ni x Mn y Co 1– x – y]O 2 Single-Crystal Cathode Materials. *ACS Appl. Energy Mater.* **2020**, *3* (12), 12238–12245. https://doi.org/10.1021/acsaem.0c02278.

(47) Lee, W.; Lee, S.; Lee, E.; Choi, M.; Thangavel, R.; Lee, Y.; Yoon, W. S. Destabilization of the Surface Structure of Ni-Rich Layered Materials by Water-Washing Process. *Energy Storage Mater.* **2022**, *44* (July 2021), 441–451. https://doi.org/10.1016/j.ensm.2021.11.006.

(48) Zhang, H.; Liu, H.; Piper, L. F. J.; Whittingham, M. S.; Zhou, G. Oxygen Loss in Layered Oxide Cathodes for Li-Ion Batteries: Mechanisms, Effects, and Mitigation. *Chem. Rev.* **2022**, *122* (6), 5641–5681. https://doi.org/10.1021/acs.chemrev.1c00327.

(49) Mu, L.; Lin, R.; Xu, R.; Han, L.; Xia, S.; Sokaras, D.; Steiner, J. D.; Weng, T. C.; Nordlund, D.; Doeff, M. M.; Liu, Y.; Zhao, K.; Xin, H. L.; Lin, F. Oxygen Release Induced Chemomechanical Breakdown of Layered Cathode Materials. *Nano Lett.* **2018**, *18* (5), 3241–3249. https://doi.org/10.1021/acs.nanolett.8b01036.

(50) Mukherjee, P.; Lu, P.; Faenza, N.; Pereira, N.; Amatucci, G.; Ceder, G.; Cosandey, F. Atomic Structure of Surface-Densified Phases in Ni-Rich Layered Compounds. *ACS Appl. Mater. Interfaces* **2021**, *13* (15), 17478–17486. https://doi.org/10.1021/acsami.1c00143.

(51) Xiao, P.; Shi, T.; Huang, W.; Ceder, G. Understanding Surface Densified Phases in Ni-Rich Layered Compounds. *ACS Energy Lett.* **2019**, *4* (4), 811–818. https://doi.org/10.1021/acsenergylett.9b00122.

(52) Tian, C.; Xu, Y.; Kan, W. H.; Sokaras, D.; Nordlund, D.; Shen, H.; Chen, K.; Liu, Y.; Doeff, M. Distinct Surface and Bulk Thermal Behaviors of LiNi0.6Mn0.2Co0.2O2 Cathode

Materials as a Function of State of Charge. *ACS Appl. Mater. Interfaces* **2020**, *12* (10), 11643–11656. https://doi.org/10.1021/acsami.9b21288.